




High-fidelity low-loss state detection of alkali-metal atoms in optical tweezer trapsMatthew N. H. Chow ^{1,2,3,*}, Bethany J. Little ¹ and Yuan-Yu Jau ^{1,2,3}¹*Sandia National Laboratories, Albuquerque, New Mexico 87185, USA*²*Department of Physics and Astronomy, University of New Mexico, Albuquerque, New Mexico 87106, USA*³*Center for Quantum Information and Control, University of New Mexico, Albuquerque, New Mexico 87131, USA*

(Received 28 September 2022; revised 12 April 2023; accepted 14 July 2023; published 7 September 2023)

We demonstrate the discrimination of ground-state hyperfine manifolds of a cesium atom in an optical tweezer using a simple probe beam with $99.91_{-0.02}^{+0.02}\%$ detection fidelity and $0.9(2)\%$ detection-driven loss of bright-state atoms. Our detection infidelity of $0.09_{-0.02}^{+0.02}\%$ is an order of magnitude better than previously published low-loss readout results for alkali-metal atoms in optical tweezers. We achieve these results by identifying and mitigating an extra depumping mechanism due to stimulated Raman transitions induced by trap light in the presence of probe light. In this work, complex optical systems and stringent vacuum pressures are not required, enabling straightforward adoption of our techniques on contemporary experiments.

DOI: [10.1103/PhysRevA.108.032407](https://doi.org/10.1103/PhysRevA.108.032407)**I. INTRODUCTION**

Neutral atoms in arrays of optical dipole traps (ODTs) provide a promising platform for quantum computing [1–3], quantum simulation [4,5], quantum chemistry [6], and optical clocks [7]. Atoms can be individually controlled inside tightly focused beams, known as optical tweezers, and have been used to generate defect-free arrays of tens to hundreds of atoms in one-, two- and three-dimensional geometries [8–11]. Alkali-metal atoms are frequently utilized because of the simplicity of their electronic structure and well-established methods of laser cooling [12].

The performance of alkali-metal atoms in tweezer platforms has, to date, been limited in part by state readout fidelity. Detection schemes are typically based on either state-dependent fluorescence collection or loss, where the state of the atom is mapped to trap occupation. Although relatively high detection fidelity has been achieved with loss-based schemes [3], these methods impose a vacuum-dependent upper bound on readout fidelity, slow the repetition rate, and complicate algorithms requiring mid-circuit measurement. On the other hand, fluorescence detection allows, in principle, for high-fidelity state measurement without losing the atom. Previous results for alkali atoms with low-loss fluorescence detection have shown no better than 1.2% infidelity without enhancement from an optical cavity [13–19]. Alternately, high-fidelity, low-loss detection of alkali atoms has been demonstrated in an optical lattice using a state-dependent potential method [20], but adaptation of this method to optical tweezers is not straightforward.

In this work, we report state discrimination between ground-state hyperfine manifolds of Cs atoms with $0.09_{-0.02}^{+0.02}\%$ infidelity while suffering only $0.9(2)\%$ detection-driven losses of the bright state atoms. We achieve this detection fidelity by mitigating a previously unreported depumping channel stemming from simultaneous probe

and trap illumination. Our low-loss rate is achieved with assistance from an adaptive detection scheme to manage detection heating. We do not impose any stringent vacuum or optical system requirements to achieve this result, enabling straightforward integration of our techniques on contemporary alkali-metal atom tweezer platforms.

This work is an important step towards scalable, high-performance alkali-tweezer machines. While the measurement error on noisy intermediate-scale quantum (NISQ) computers is often overlooked as it does not typically scale with algorithm length, it is important to consider the (generally exponential) scaling of the measurement error with system size. In addition, by demonstrating simultaneous high-fidelity and low loss, we improve the outlook for quantum sensing applications where the sensitivity is tied to atom retention capability via repetition rate.

II. EXPERIMENT

Our experiment sequence begins by monitoring collected fluorescence with a field programmable gate-array (FPGA) control system and triggering the pulse program when we detect that a Cs atom has been loaded from the magneto-optical trap into a tweezer trap. As shown in Fig. 1, the tweezer is formed by focusing up to 10 mW of linearly polarized laser light through a 0.45 numerical aperture (NA) microscope objective (OptoSigma PAL-20-NIR-LC00) to a spot with a $1.6\ \mu\text{m}$ $1/e^2$ waist radius. The trap is small enough that a light-assisted collisional-blockade mechanism ensures loading no more than one atom at a time [21]. The trap wavelength of $\lambda_{\text{trap}} = 937\ \text{nm}$ is chosen to be red-detuned from both the D_1 and D_2 line transitions and to have approximately the same ac Stark shift on both states ($6S_{1/2}$ and $6P_{3/2}$) of the cooling transition (i.e., “magic”). After loading an atom, we cool it with polarization-gradient cooling to $\approx 10\ \mu\text{K}$. We then apply a bias magnetic field of 4 G along the x direction, and we prepare the atom in either the $|F = 4\rangle$ (“bright”) or $|F = 3\rangle$ (“dark”) hyperfine ground manifold via optical pumping with

*mnchow@sandia.gov

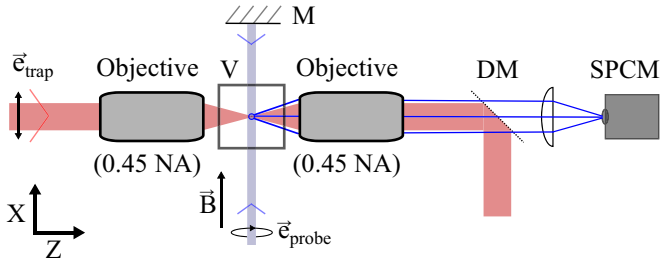


FIG. 1. We use a simple probe beam and fluorescence collection optical system to measure high-fidelity state detection. Both the probe beam (blue shaded line) propagation direction and trap light (red shaded line) polarization (\vec{e}_{trap}) are oriented along the bias magnetic-field direction (\vec{B}). The probe is right-hand circularly polarized to drive only σ_+ transitions. The probe is retroreflected with a gold mirror (M) to minimize polarization distortions. Fluorescence (blue rays) is collected outside of the vacuum chamber (V) with a 0.45-NA microscope objective, separated from the trap light with a dichroic mirror (DM), and focused onto a single-photon counting module ($SPCM$).

either a D_2 line $F = 3$ to $F' = 4$ repump beam or D_1 line $F = 4$ to $F' = 4$ depump beam, respectively. Finally, the state of the atom is read out using a near-resonant probe laser, and we check for atom retention in the trap with the cooling beams.

When preparing the bright state, a circularly polarized beam tuned near the $F = 4$ to $F' = 5$ D_2 line transition (the same beam that is later used as the probe) is turned on during the final $10\ \mu\text{s}$ of pumping with the repump to prepare the atom in the $F = 4$, $m_F = 4$ “stretched” state. We choose to use the stretched state as the bright qubit level to suppress off-resonant scatter from the probe beam during detection. The detection protocol works with other Zeeman states (or mixtures of Zeeman states) within the $F = 4$ manifold as well, but suffers a small (order 10^{-4} for our settings) penalty of increased bright-state depumping probability during the first few scattering events of detection, as the suppression of off-resonant scattering gained from angular momentum conservation only takes effect once the atom reaches the Zeeman-specific closed cycling transition subspace (see Appendix B) [15]. No Zeeman level control is applied when preparing the atom in the $F = 3$ hyperfine manifold.

During detection, we use a near-resonant probe beam that is tuned to the $F = 4$ to $F' = 5$ D_2 line transition so that the $F = 4$, bright ground-state scatters probe photons in a closed cycling transition, while the $F = 3$ state is dark to the probe and ideally scatters no light. The intensity of the probe is $0.40(1) I_{\text{sat}}$, where I_{sat} is the saturation intensity on the $|F = 4, m_F = 4\rangle \rightarrow |F' = 5, m'_F = 5\rangle$ transition. Detuning of the probe is $2\pi \times 0.26(3)$ MHz red of the same line, which is chosen empirically to maximize survival probability while still maintaining a high scattering rate. State-dependent fluorescence is then collected and imaged onto a single photon counting module (SPCM, Excelitas SPCM-AQRH-16), which is monitored in real time by our FPGA control system. The atom is assigned a label, bright or dark, based on a discrimination threshold level of collected photon counts. The probe beam is right-hand circularly polarized and a bias magnetic

field of 4 G is set along its propagation direction such that we drive primarily σ_+ transitions.

To mitigate atom loss induced by photon recoil during detection [22,23], we retroreflect the probe beam [24] to balance the scattering force. We also implement an adaptive detection scheme where we apply our probe laser in a series of $5\text{-}\mu\text{s}$ pulses until either the threshold number of photons is collected or we reach our maximum probe duration of $250\ \mu\text{s}$ [14,25–29]. Since extra photons beyond threshold provide no additional information in a thresholding detection scheme, this effectively eliminates extraneous heating at no cost to the state discrimination fidelity. See Appendix C for more details.

In an ideal scenario, we would be able to determine the state of the atom with arbitrary accuracy by collecting scattered photons until the bright and dark count distributions are sufficiently separated. However, recoil heating of the bright state during detection limits the maximum possible probe time before atom loss, and depumping from trap and probe light can lead to state information loss during detection. We study three depumping mechanisms, illustrated in Fig. 2: (a) off-resonant scatter of trap light, (b) probe polarization components that allow for off-resonant scatter via $F' \neq 5$, and (c) trap-induced two-photon coupling of excited-state hyperfine manifolds via stimulated Raman transitions. The first mechanism is the main fundamental constraint, and can be mitigated by improving the ratio of photon collection to trap off-resonant scattering rates. The second mechanism is imposed by probe misalignment and polarization impurity, and can be improved with further technical capability. The third is an almost entirely geometrical problem and can be essentially eliminated by an appropriate choice of trap polarization, bias fields, probe polarization, and probe propagation direction. To our knowledge, this third information loss channel has not been previously reported for this type of detection, and mitigation of this depumping pathway is critical to achieving the state discrimination fidelity observed in our work.

III. ANALYSIS OF INFORMATION LOSS DURING DETECTION

To guide our choice of detection parameters, we use a statistical model of photon collection governed by the rates of three processes: The count collection rate from a bright atom, the dark collection rate (background), and the rate of state-information loss from the prepared state of the atom (the depump rate). We use a short detection time compared to the depump rate and thus consider at most a single state change event during detection [30]. The resulting photon collection distribution is found by marginalizing over state change event times, t :

$$P(n) = e^{-t_d R_{\text{dep}}} \mathcal{P}(n, R_p t_d) + \int_0^{t_d} \mathcal{P}(n, R_p t + R_{np}(t_d - t)) R_{\text{dep}} e^{-t R_{\text{dep}}} dt. \quad (1)$$

Here, $P(n)$ is the probability of detecting n photons, $\mathcal{P}(n, Rt) = e^{-Rt} (Rt)^n / n!$ is the probability of n events in a Poisson distribution of mean Rt , t_d is the total detection time, R_p is the photon collection rate from an atom in the prepared

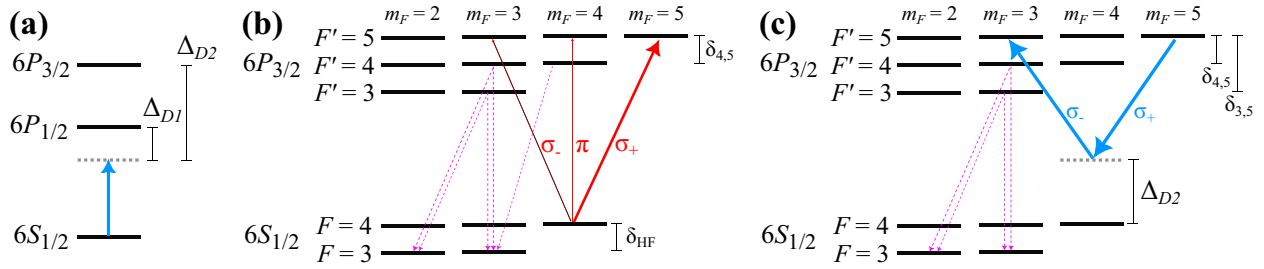


FIG. 2. Three mechanisms contribute to state information loss during detection. (a) The fundamental limitation of effective T_1 relaxation in an optical dipole trap is imposed by the off-resonant scattering rate from the light used to generate the trapping potential (solid blue line). For trapping parameters used in this paper [$U_0/h = 8.9(2)$ MHz], T_1 is measured to be $0.49(3)$ s. (b) Probe (solid red lines) polarization impurities and misalignment to the magnetic field axis allow for weak, off-resonant coupling to $F' \neq 5$ excited-state hyperfine manifolds, which then have dipole-allowed decay channels (dashed lines) to the $F = 3$ ground-state manifold. (c) σ_{\pm} trap light (solid blue lines) allows for detuned, two-photon coupling from $F' = 5$ to $F' \neq 5$ excited-state hyperfine manifolds. This depumping mechanism can be effectively eliminated by using π -polarized trap light, for which there is no allowed two-photon transition to any $m'_F \neq 5$ excited state from the $|6P_{3/2}, F' = 5, m'_F = 5\rangle$ level. Only one two-photon pathway using the ground state as an intermediate level with σ_{\pm} -polarized trap light is depicted here as an example; other intermediate states (primarily $6D$ and $7S$ states) also contribute to the total effective Raman Rabi rate (see Appendix D). Levels not drawn to scale.

state, R_{np} is the collection rate from the atom after a state changing event (i.e., collection rate from the nonprepared state), and R_{dep} is the depumping rate out of the prepared state. The first term represents the contribution from cases where no depumping occurs, and the second term is the convolution of counts from before and after a state change event.

Thresholding at m detected counts to assign state labels, we define the bright label probability as a function of F , the prepared state: $P_{\text{bright}}(F) = \sum_{n=m}^{\infty} P(n|F)$. The bright-state readout error is the probability of failing to assign a bright label to an atom prepared in the bright state: $\varepsilon_{\text{bright}} = 1 - P_{\text{bright}}(F = 4)$, and similarly the dark state readout error is the probability of assigning a bright label to an atom prepared in the dark state: $\varepsilon_{\text{dark}} = P_{\text{bright}}(F = 3)$. For all infidelities quoted in this work, we use $\mathcal{I} = \frac{1}{2}(\varepsilon_{\text{bright}} + \varepsilon_{\text{dark}})$, and all fidelities are $\mathcal{F} = 1 - \mathcal{I}$. For the range of collection and depumping rates near our experiment parameters, we numerically find $m = 3$ to be the optimal discrimination threshold.

The background photon collection rate is $5.2(3) \times 10^2 \text{ s}^{-1}$ and the bright atom collection rate is $5.44(3) \times 10^4 \text{ s}^{-1}$, such that, for $m = 3$, optimal error rates of $\varepsilon_{\text{bright}} = 0.005\%$ and $\varepsilon_{\text{dark}} = 0.04\%$ would be achieved in an ideal, depump-free, case at 0.26 ms of probe time. However, observed error rates are significantly higher (especially for the bright state), indicating that state information loss during detection is the dominant source of detection infidelity. As a figure of merit, we consider the rate of information loss, R_{dep} , compared to the rate of information gain, R_{bright} : $\mathcal{R} = R_{\text{dep}}/R_{\text{bright}}$. \mathcal{R} is the depump probability per collection event from the bright state. As a rough approximation for estimating fidelity, one can consider the probability of collecting m photons from the bright state prior to depump, $(1 - \mathcal{R})^m \approx 1 - m\mathcal{R}$ for $m\mathcal{R} \ll 1$.

A. Single-photon depumping from off-resonant scattering

We begin our analysis of state information loss during detection by considering single-photon off-resonant scattering from the trapping laser, illustrated in Fig. 2(a). Using a nu-

meric density matrix model including all magnetic levels of the ground and first excited states ($6P_{1/2}$ & $6P_{3/2}$), we find that the depumping rate from the trap light is $R_{\text{dep,trap}} \approx 2.5 \times 10^{-7} U_0/h$, where U_0 is the trap depth and h is Planck's constant [31]. For a trap depth of $U_0/h = 8.9(2)$ MHz, this yields an effective $T_1 = 1/R_{\text{dep,trap}}$ of 0.45 s and a normalized depump rate of $\mathcal{R}_{\text{trap}} = 4.1 \times 10^{-5}$. To experimentally verify, we measure exponential decay times for the bright [dark] state and find $0.41(3)$ s [$0.58(3)$ s] [32].

The probe beam may also cause state information loss due to off-resonant scatter, as illustrated in Fig. 2(b). Although we attempt to drive only σ_+ transitions with the probe beam, polarization impurity or misalignment of the probe propagation direction to the magnetic field allows for off-resonant scatter via $F' \neq 5$ levels. Following the calculation in Ref. [15], we find the depump rate by summing over all dipole-allowed transition scattering rates, weighted by the branching ratio (b_{α}) of each excited state ($|\alpha\rangle$) to the $F = 3$ ground-state manifold.

The sum depends on probe polarization purity, alignment to the magnetic field, and intensity. Our measured degree of probe polarization is 99.4% out of the fiber launch [33], and the probe reflects off of a single unprotected gold mirror before entering the vacuum chamber. We align the magnetic field by scanning shim fields and maximizing the bright label probability for atoms prepared in $F = 4$ after a conservatively long detection time, such that we expect an alignment tolerance of a few degrees and resulting σ_- - and π -polarization intensity fractions of $\leq 2\%$. This corresponds to an expected probe off-resonant scatter rate of $\leq 2.3 \text{ s}^{-1}$ or $\mathcal{R}_{\text{probe}} \leq 5.1 \times 10^{-5}$, comparable to the depump probability due to the trap off resonant scatter. See Appendix A for the full calculation.

However, for an arbitrary trap polarization orientation relative to the quantization axis, the above single-photon mechanisms alone are insufficient to explain observed depumping rates. A trap-light driven, detuned, two-photon effect, illustrated in Fig. 2(c), provides another pathway for atoms to escape the cycling transition subspace. While the ground-state hyperfine splitting of ≈ 9.2 GHz is sufficiently large to prevent significant Raman transitions between ground-state

manifolds, the excited-state hyperfine splitting is only of order 100 MHz. For some choices of experiment geometry, this leads to appreciable population leakage of excited state atoms to $F' \neq 5$ by detuned Raman transitions through the ground state and higher-lying excited states, as calculated in the following section.

B. Two-photon depumping induced by trap light

For illustration of the two-photon depumping mechanism, we consider the scenario where the bias magnetic field is orthogonal to the polarization direction of the linearly polarized trap beam. For this case, σ_+ and σ_- polarization components with equal electric field amplitude $\mathcal{E}_+ = \mathcal{E}_- = \mathcal{E}/\sqrt{2}$ are generated by the trap light. When the optical detuning is much larger than the two-photon detuning ($\Delta \gg \delta$), the effective two-photon transition Rabi frequency $\Omega_{\text{eff},F'}$ for final state $|6P_{3/2}, F'\rangle$ caused by the σ_+ and σ_- transitions can be found by summing the effective two-photon Rabi frequency through each intermediate level ($\Omega_{\text{eff},F',i}$) [34]

$$\Omega_{\text{eff},F'} = \sum_i \Omega_{\text{eff},F',i} = \sum_i \frac{\Omega_{+,i}\Omega_{-,i}}{2\Delta_i}, \quad (2)$$

where Δ_i is the trap laser detuning from intermediate level, $|i\rangle$, $\Omega_{+,i}$ ($\Omega_{-,i}$) is the optical Rabi rate for each arm $|i\rangle$ to $|F' = 5, m'_F = 5\rangle$ ($|F', m'_F = 3\rangle$) of the two-photon Raman transition, and the sum is carried out over all intermediate states. If $\Omega_{\text{eff},F'}$ is strong enough, the population transfer between $|F' = 5, m'_F = 5\rangle$ and $|F' = 4$ or $3, m'_F = 3\rangle$ caused by the Raman transition can be nonnegligible even when these hyperfine sublevels are separated by hundreds of MHz (i.e., largely RF detuned). For state detection, the probing time scale is usually much longer than the decoherence rate γ_c of the superposition state of the excited-state sublevels. Solving the optical Bloch equation [31] we find the late-time ($t \gg 1/\gamma_c$), mutual population transfer rate to be

$$\Gamma_{R,F'} = \frac{\Omega_{\text{eff},F'}^2}{2(\delta_{F',5}^2 + \gamma_c^2)} \gamma_c. \quad (3)$$

When the probe is present, the population ($\rho_{5',5'}$) in the source sublevel ($|F' = 5, m'_F = 5\rangle$) is nonzero, and we find the target sublevel ($|F', m'_F\rangle$) quasisteady population to be

$$\rho_{F',m'_F} = \frac{\Gamma_{R,F'}}{\Gamma_{R,F'} + \Gamma_s} \rho_{5',5'}, \quad (4)$$

where Γ_s is the excited-state decay rate due to spontaneous emission. In our case, $\gamma_c = \Gamma_s$. Thus, for $\delta \gg \gamma_c$, we find

$$\rho_{F',m'_F} \approx \frac{\Omega_{\text{eff},F'}^2}{2\delta_{F',5}^2 + \Omega_{\text{eff},F'}^2} \rho_{5',5'}. \quad (5)$$

To calculate the Raman Rabi rate $\Omega_{\text{eff},F'}$ from a measured quantity, we find that $\Omega_{\text{eff},F',i}$ can be derived from the trap depth, U_0 , of the far-detuned optical dipole trap (see Appendix D for derivation)

$$\Omega_{\text{eff},F',i} = a_{F',i} \frac{2U_0}{\hbar\Delta_i} \left| \frac{\Delta_{D_1}\Delta_{D_2}}{\Delta_{D_1} + (f_{D_1}/f_{D_2})\Delta_{D_2}} \right|, \quad (6)$$

where $a_{F',i}$ is a prefactor derived from angular momentum coupling coefficients dependent on the intermediate and final

states, \hbar is the reduced Planck constant, $\Delta_{D_1(D_2)}$, and $f_{D_1(D_2)}$ are the detuning and oscillator strength for the $D_1(D_2)$ line transition. As a concrete example, when considering the transition to the $F' = 4$ excited state using the ground state as an intermediate level [as depicted in Fig. 2(c)], $a_{F',i} = -\sqrt{\frac{21}{320}}$. This yields an effective Raman Rabi rate of

$$\Omega_{\text{eff},4',i|i=6S_{1/2}} \approx 2\pi \times \left(-0.255 \frac{U_0}{h} \right) \quad (7)$$

for 937-nm trap light. By taking the (signed) sum of the effective Raman Rabi rates through all nearby intermediate levels (S orbitals with principle quantum numbers 6 to 9 and D orbitals with principle quantum numbers 5 to 7, see Tables III to V in Appendix D) we arrive at

$$\Omega_{\text{eff},4'} \approx 2\pi \times \left(-0.278 \frac{U_0}{h} \right). \quad (8)$$

Using our trap depth of $U_0/h = 8.9$ MHz and $\delta_{4,5}/2\pi = 251$ MHz two-photon detuning [35], we find the population $\rho_{4',3'}$ according to Eq. (5) to be $\rho_{4',3'} \approx \rho_{5',5'} \times 9.7 \times 10^{-5}$. The branching ratio of the $F' = 4$ manifold to the $F = 3$ ground state is $b_{4'} = 5/12$ [15], so the overall probability of depumping per resonant scattering event for this transition is

$$p_{\text{depump},4',3'} = b_{4'} \frac{\rho_{4',3'}}{\rho_{5',5'}} \approx 4.1 \times 10^{-5}. \quad (9)$$

A similar calculation can be carried out for the two photon transition to $|F' = 3, m'_F = 3\rangle$:

$$\Omega_{\text{eff},3'} \approx 2\pi \times \left(0.359 \frac{U_0}{h} \right); \quad (10)$$

$$\frac{\bar{\rho}_{3',3'}}{\bar{\rho}_{5',5'}} \approx 5.0 \times 10^{-5} \quad (\text{for } U_0/h = 8.9 \text{ MHz}); \quad (11)$$

$$p_{\text{depump},3',3'} = b_{3'} \frac{\bar{\rho}_{3',3'}}{\bar{\rho}_{5',5'}} \approx 3.7 \times 10^{-5}. \quad (12)$$

Combining these two depump probabilities, we have a 7.8×10^{-5} chance of depump for each resonant scattering event with this configuration, or $\mathcal{R}_{\text{Raman}} \approx 8.1 \times 10^{-3}$ after accounting for our collection efficiency (CE) of 0.96(1)%, which is a measured value that includes transmission of our optical system and the quantum efficiency of the detector.

For the calculation illustrated here, we only consider the case of σ_+ - σ_- Raman transitions. For other configurations of the trap-light polarization and the bias magnetic field, π - σ_- and/or π - σ_+ Raman transitions can also exist. Mathematical treatments can be found through a similar procedure.

To verify this newly identified mechanism, we experimentally study the bright-state count histogram for two geometries. We orient the quantization axis, jointly defined by the magnetic field and the probe propagation direction, either parallel or orthogonal to the trap polarization generating either π or σ_{\pm} polarization components of the trapping beam. With the σ -polarized trap light, we expect to see depumping from the two-photon pathway as calculated. However, for the π -polarized trap configuration, there is no dipole-allowed two-photon coupling from $|F' = 5, m'_F = 5\rangle$ to any $m'_F \neq 5$ level caused by the trap light due to the selection rule $\Delta m_F = 0$ for π polarization. Therefore, we expect this mechanism to be

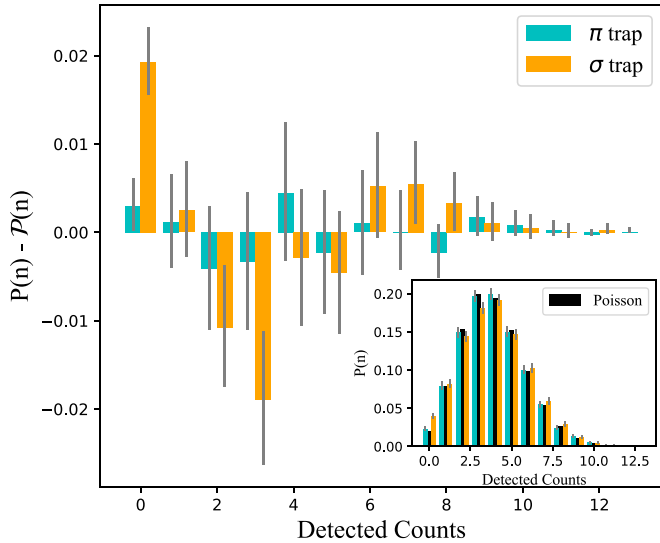


FIG. 3. Bright-state detection count histograms for different experiment geometries demonstrate the effect of two-photon depumping from the trap light. In the main figure, we take the difference of detection count histograms for a fixed probe duration, $P(n)$, and the depump-free case of a Poisson distribution with the same mean $\mathcal{P}(n)$. Full histograms are shown in the inset. The distribution collected using the σ -polarized configuration (orange bars) is significantly non-Poissonian and has a substantially larger zero counts bin than that of the π -polarized configuration (teal bars). This indicates a higher depump rate in the σ -polarized configuration that we attribute to Raman transitions from the trap light. When the trap has σ_{\pm} components, two-photon coupling between excited manifold hyperfine states allows for leakage out of the cycling transition subspace, while in the π -polarized trap configuration, the lack of dipole-allowed coupling to $m'_f \neq 5$ states prevents two-photon leakage during bright-state detection. There are 10 000 shots in each data histogram; uncertainty markers are Wilson score intervals.

absent (barring trap polarization misalignment and polarization distortion effects from focusing).

As shown in Fig. 3, we run an illustrative experiment comparing these two configurations and find that the histogram of collected light from a bright atom in a π -polarized trap is significantly closer to the ideal depump-free Poisson distribution than that of an atom in a σ -polarized trap [36]. A fit to Eq. (1) yields depumping probabilities per scattering event of $50(5) \times 10^{-6}$ and $7(4) \times 10^{-6}$ for the σ and π configurations, respectively. Uncertainties here are fitting uncertainties. Since the other probe and trap parameters are held fixed, we infer the difference in the depump rates between the two configurations to be caused by off-resonant Raman transitions. These data were taken prior to a significant optimization of the probe beam optics, and we attribute the remaining depump rate in the π configuration mostly to probe imperfections.

IV. RESULTS AND DISCUSSION

We measure our detection fidelity in a π -polarized trap by preparing the atom in each state 100 000 times and recording the number of times that the measured state matches the prepared state. In Fig. 4, we show data that were collected in 1000 batches of 100 shots, alternating between bright- and

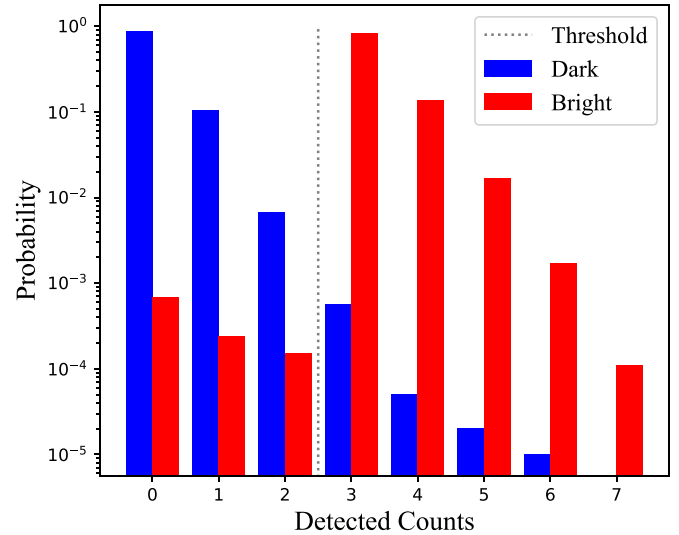


FIG. 4. The normalized histogram of collected photons from the bright and dark state demonstrates $0.09^{+0.02}_{-0.02}\%$ detection infidelity. Single atoms are prepared in either the dark (blue) or bright (red) state and read out by illuminating the atom with the D_2 line probe for up to $250 \mu\text{s}$ and collecting scattered photons. When three or more photons are collected, the atom is labeled bright; when fewer than three photons are collected, the atom is labeled dark. Atoms prepared in the bright state are erroneously labeled dark in $0.11^{+0.03}_{-0.02}\%$ of experiments, and atoms prepared in the dark state are erroneously labeled bright in $0.06^{+0.02}_{-0.01}\%$ of experiments. Data presented in this histogram were collected in 1000 batches of 100 shots, alternating between dark and bright state preparation, for a total of 100 000 shots for each state.

dark-state preparation for each batch. A total of 107 trials where the atom was prepared in the bright state were read out as dark, and 64 trials where the atom was prepared in the dark state were read out as bright. Stated as percentages, this is a bright error of $\varepsilon_{\text{bright}} = 0.11^{+0.03}_{-0.02}\%$ and a dark error of $\varepsilon_{\text{dark}} = 0.06^{+0.02}_{-0.01}\%$, yielding an infidelity of $0.09^{+0.02}_{-0.02}\%$ or a fidelity of $99.91^{+0.02}_{-0.02}\%$. Uncertainties given here are Wilson score intervals. The fidelity reported here is a conservative lower bound on the detection fidelity, as our measurement does not correct for state preparation errors. We expect our state preparation error to be small compared to the readout error based on our measured pumping time constants and optical pumping duration. We then infer the detection-driven loss probability by subtracting the ratio of the probability of passing the presence check when preparing in the bright and dark state from unity: $\tilde{P}_{\text{loss}} = 1 - P_{\text{survive},4}/P_{\text{survive},3}$, where \tilde{P}_{loss} is the probability of losing a bright state atom due to detection and $P_{\text{survive},F}$ is the total atom retention probability when preparing in state F . We find $\tilde{P}_{\text{loss}} = 0.9(2)\%$.

To compare to the predicted depumping rate, we calculate the total depump probability per collection event from the bright state error and find $\mathcal{R} = 1 - \sqrt[3]{1 - \varepsilon_{\text{bright}}} = 3.7 \times 10^{-4}$. This value is within an order of magnitude of the sum of estimated contributions from off-resonant scatter from probe and trap light. The source of any remaining discrepancy in the observed depump rate is a subject of ongoing study. Possible sources of contribution to observed error rates include

imperfect state preparation, overestimation of probe alignment or purity, failed presence checks resulting in poor quality postselection, and residual σ -polarized components of the trap light due to misalignment of the trap polarization direction to the magnetic field or polarization distortion effects due to focusing of the trap beam.

This depump rate is sufficiently low to permit high-fidelity detection even in the case of low collection efficiency optical systems. When we fiber-coupled our atomic fluorescence, we still achieved $99.84^{+0.02}_{-0.03}\%$ fidelity and 2.6(2)% detection-driven loss of the bright state, even though the collection efficiency was only 0.37%. In such a system with low depump rates and low collection efficiency, detection heating losses play a more dominant role. We found that, to some degree, we could trade atom survival probability for detection fidelity and reach a detection fidelity of $99.89^{+0.02}_{-0.02}\%$ with 14.1(3)% loss of the bright-state atoms due to detection.

To test the applicability of our result to atom-array imaging, for which adaptive detection would be challenging using a typical camera due to slow data transfer and processing, we also measure the detection fidelity and detection-driven loss of the bright state without using adaptive detection. We reduce the probe intensity and use a probe time of 350 μ s to achieve a bright error of $\varepsilon_{\text{bright}} = 0.22^{+0.03}_{-0.03}\%$ and a dark error of $\varepsilon_{\text{dark}} = 0.13^{+0.02}_{-0.02}\%$ for a combined readout infidelity of $0.18^{+0.02}_{-0.02}\%$. We observe 1.8(3)% detection-driven loss of the bright state atoms. See Fig. 5 for the full histogram [37].

We note that further improvement of the detection fidelity and atom retention should be achievable by improving the photon collection efficiency since our measured collection efficiency of 0.96(1)% is relatively poor compared to other works [15,16]. We also note that these results ease vacuum system requirements for high-fidelity detection of alkali atoms in optical tweezers since detection fidelity is independent of the background atom loss rate. To achieve comparable fidelities with a pushout method, the average atom loss rate due to background gas collisions (or indeed any source other than the pushout beam) must be comparable to the readout error reported here since a dark atom lost due to background is indistinguishable from a bright atom lost to the pushout beam in such schemes. Finally, we note that our result obviates the need for toggling the trap and probe beams, as we keep the trap beam on at all times and still achieve high fidelity. Use of a magic wavelength trap is important for our ability to keep the trap on, as we avoid dipole force fluctuation (DFF) heating [22]. Toggling the trap and probe beam could be an alternate strategy to mitigate both the two-photon depumping mechanism and DFF heating, at the cost of potentially introducing an extra heating mechanism from repeated kicks.

Ultimately, the fidelity reported here is the result of study of the relevant atom-photon interaction physics and mitigation of a previously unreported depumping mechanism under simultaneous trap and probe illumination. We find that the remaining infidelity from off-resonant scattering of trap and probe light is sufficiently low to enable an order of magnitude improvement over previously published low-loss readout of alkali atoms in optical tweezers. In conjunction with the high atom retention enhanced by adaptive detection, this result alludes to the promise of near-term detection suitable for fault tolerant operation and the possibility of

nondestructive mid-circuit measurement for error detecting or correcting algorithms. This work represents an important step towards building scalable, high-performance quantum information processors and quantum sensors out of alkali-metal atoms trapped in optical tweezers.

ACKNOWLEDGMENTS

We thank Paul Parazzoli, Ivan Deutsch, Justin Schultz, and Vikas Buchemavari for helpful discussions. We also thank a member of the peer review process who suggested we add additional levels to our two-photon depumping calculations, which resulted in a small numerical correction. This work was supported by the Laboratory Directed Research and Development (LDRD) program at Sandia National Laboratories. Sandia National Laboratories is a multimission laboratory managed and operated by National Technology & Engineering Solutions of Sandia, LLC, a wholly owned subsidiary of Honeywell International Inc., for the U.S. Department of Energy's National Nuclear Security Administration under Contract No. DE-NA0003525. This paper describes objective technical results and analysis. Any subjective views or opinions that might be expressed in the paper do not necessarily represent the views of the U.S. Department of Energy or the United States Government.

During publication of this work, nondestructive readout exceeding 99% fidelity was achieved on an array of alkali atoms in [38] and on alkaline-earth atoms in [39].

APPENDIX A: PROBE OFF-RESONANT SCATTER RATE

The calculation of the single-photon off-resonant scattering rate is done following Ref. [15]. Here, the atom is assumed

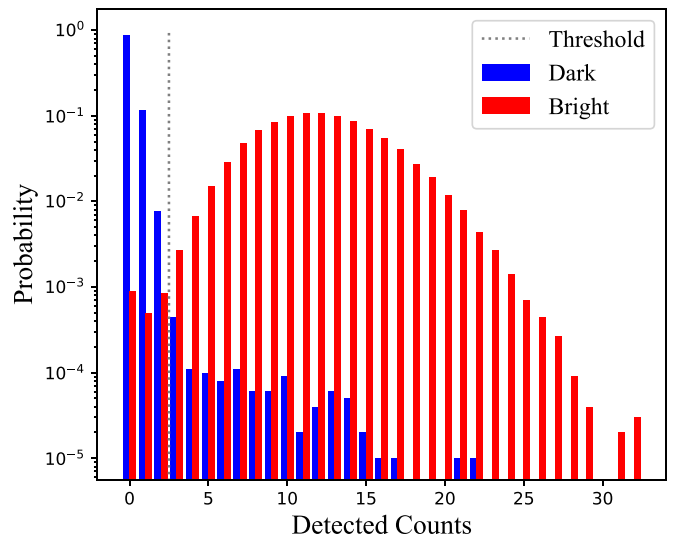


FIG. 5. The normalized histogram of collected photons from bright and dark state atoms as measured without adaptive detection demonstrates $0.18^{+0.02}_{-0.02}\%$ detection infidelity. Data presented in this histogram were collected in 1000 batches of 100 shots, alternating between dark and bright state preparation, for a total of 100 000 shots for each state.

to start in the stretched ground state ($|F = 4, m_F = 4\rangle$) and we calculate the equilibrium population in each excited state ($|F', m'_F\rangle$) under probe light illumination. The depump rate is then calculated by summing the scattering rate on each excited state (R_{scat,F',m'_F}) that is reachable with a dipole-allowed transition, scaled by their branching ratios to the dark ground-state manifold ($b_{F'}$) [15,40]

$$R_{\text{scat},F',m'_F} = \Gamma \frac{\Omega_{F',m'_F}^2}{\Gamma^2 + 2\Omega_{F',m'_F}^2 + 4\delta_{F',m'_F}^2}, \quad (\text{A1})$$

$$R_{\text{dep,probe}} = \sum_{F',m'_F} b_{F'} R_{\text{scat},F',m'_F}, \quad (\text{A2})$$

where Γ is the natural linewidth of the D_2 transition, δ_{F',m'_F} is the probe laser detuning from $|F', m'_F\rangle$, and $\Omega_{F',m'_F} \equiv \Omega_{F',m'_F,F,m_F}|_{F=4,m_F=4}$ is the optical Rabi rate associated with the transition from state $|F = 4, m_F = 4\rangle$ to state $|F', m'_F\rangle$. We find the D_2 optical transition Rabi frequency between a ground-state hyperfine sublevel $|F, m_F\rangle$ and a excited-state hyperfine sublevel $|F', m'_F\rangle$ to be [15,31]

$$\Omega_{F',m'_F,F,m_F} = \sqrt{\frac{2}{3}} \frac{\mathcal{E}_q d}{\hbar} \times (-1)^{2F'+F-q+7} \sqrt{(2F+1)(2J+1)} \\ \times \begin{Bmatrix} J & I & F \\ F' & 1 & J' \end{Bmatrix}_{6j} C_{F,m_F,1,q}^{F',m'_F}, \quad (\text{A3})$$

where \mathcal{E}_q is the spherical component of the electric field with polarization $q = m'_F - m_F$, $F = 4$ (F'), and $J = 1/2$ ($J' = 3/2$) are the ground (excited) state hyperfine and total electron angular momentum quantum numbers, $I = 7/2$ is the nuclear spin, $C_{F,m_F,1,q}^{F',m'_F}$ is a Clebsch-Gordan coefficient, and $\{\}_{6j}$ is a Wigner-6j symbol. We use the subscripts $\{-, z, +\}$ to denote $q = \{-1, 0, +1\}$. The electric dipole moment d is calculated as

$$d = e \int_0^\infty P_{n'l'J'}^*(r) r P_{n'lJ}(r) dr. \quad (\text{A4})$$

Here, e is the unit charge and $P_{n'lJ}(r)$ is the normalized radial wave function. For the Cs D_2 transition, we have $n = 6$, $l = 0$, $J = 1/2$ as $6S_{1/2}$ and $n' = 6$, $l' = 1$, $J' = 3/2$ as $6P_{3/2}$ [41].

The Rabi rates for transitions driven by probe polarization components ($q \in \{-1, 0\}$) may then be written in terms of a polarization intensity ratio ($\tilde{I}_q = |\mathcal{E}_q|^2/|\mathcal{E}_+|^2$), a state-dependent coefficient (ξ_{F',m'_F}), and the Rabi rate on the stretched state transition ($\Omega_{5',5'}$). This expression is

$$|\Omega_{F',m'_F}|^2 = \tilde{I}_q \xi_{F',m'_F} |\Omega_{5',5'}|^2, \quad (\text{A5})$$

where

$$\xi_{F',m'_F} = \frac{\left| C_{F,m_F,1,q}^{F',m'_F} \begin{Bmatrix} J & I & F \\ F' & 1 & J' \end{Bmatrix}_{6j} \right|^2}{\left| C_{4,4,1,1}^{5,5} \begin{Bmatrix} \frac{1}{2} & \frac{7}{2} & 4 \\ 5 & 1 & \frac{3}{2} \end{Bmatrix}_{6j} \right|^2} \\ = 36 \left| C_{F,m_F,1,q}^{F',m'_F} \begin{Bmatrix} J & I & F \\ F' & 1 & J' \end{Bmatrix}_{6j} \right|^2. \quad (\text{A6})$$

Numerical values of ξ_{F',m'_F} are summarized in Table I for the relevant transitions. We numerically carry out the sum

TABLE I. Summary of relevant parameters for the calculation of probe-driven off-resonant coupling to the $|F = 4, m_F = 4\rangle$ ground state. F' and m'_F specify the excited-state sublevel, $\delta_{F'}/2\pi$ is the detuning of the probe beam from that transition, $b_{F'}$ is the branching ratio to the $F = 3$ ground-state manifold, and ξ_{F',m'_F} is the angular momentum coupling coefficient normalizing the transition strength to that of the $|F = 4, m_F = 4\rangle \rightarrow |F' = 5', m'_F = 5'\rangle$ transition, as specified in Eq. (A6). The probe is mostly σ_+ polarized, pumping the population into $|F = 4, m_F = 4\rangle$, so only excited states with dipole-allowed coupling to $|F = 4, m_F = 4\rangle$ and nonzero $b_{F'}$ are considered. Detunings are taken from Ref. [35] assuming a resonant probe and no Zeeman splitting. Branching ratios are calculated from the transition strengths given in Ref. [40] and confirmed with a formula in Ref. [15]. Values for ξ_{F',m'_F} are calculated in MATHEMATICA.

F', m'_F	Polarization	$\delta_{F'}/2\pi$ (MHz)	$b_{F'}$	ξ_{F',m'_F}
4, 4	π	251.00(2)	5/12	7/15
4, 3	σ_-	251.00(2)	5/12	7/60
3, 3	σ_-	452.24(2)	3/4	7/36

in Eq. (A2) using probe detuning of $\delta_{5',5'}/2\pi = -0.26$ MHz from the target transition (the detuning used in Sec. IV) for a range of polarization intensity ratios and total intensities. The results from these calculations are shown in Fig. 6.

We measure the probe light to have 99.4% degree of polarization out of the fiber launch (before incidence on the gold mirror) and use a polarimeter to maximize the σ_+ -polarized component. Other possible contributions to polarization imperfections come from the 45° angle of incidence on an unprotected gold mirror (Thorlabs PF05-03-M03), and any potential angular misalignment between the probe propagation direction and the bias magnetic field (B -field). The gold mirror has a specified nominal reflectance difference of 1.4% at 852 nm for S - versus P -polarized light, which leads to a small σ_- component. We find the magnitude of this component by taking the mirror to be a partially polarizing reflector, with the Jones matrix

$$M = \begin{bmatrix} \sqrt{r_s} & 0 \\ 0 & -\sqrt{r_p} \end{bmatrix} \quad (\text{A7})$$

in the s - p basis, where r_s (r_p) is the reflectance for S -polarized (P -polarized) light. We then take the input state to be pure σ_+ -polarized, calculate the renormalized output state, and project it onto the σ_- basis vector. This yields an intensity fraction of σ_- light relative to total intensity

$$\frac{I_-}{I} = \frac{r_s + r_p - 2\sqrt{r_s r_p}}{2(r_s + r_p)}. \quad (\text{A8})$$

For the gold mirror's expected reflectance, $r_s = 0.98031837$, $r_p = 0.96616158$, and $I_-/I \approx 1.3 \times 10^{-5}$.

For small misalignment angle θ between the probe propagation direction and the B -field, there is a $\sin(\theta)/\sqrt{2} \approx \theta/\sqrt{2}$ π -polarized component and $[\cos(\theta) - 1]/2 \approx -\theta^2/4$ σ_- -polarized component of the electric field. We conservatively estimate our mechanical angular tolerance to be $\leq 10^\circ$, contributing at most $\approx 1.5\%$ and $\approx 0.006\%$ to the π and σ_- intensity ratios, respectively. Thus, π -polarization components constitute the bulk of the polarization imperfections from tilt misalignment. Evaluating Eq. (A2) using

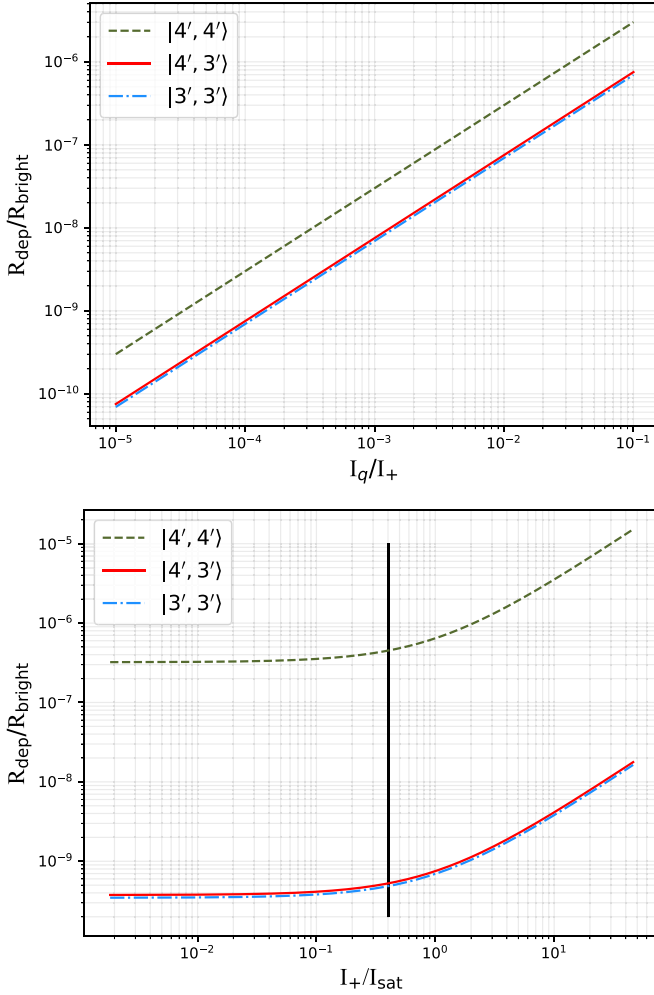


FIG. 6. Numerical results for the probe off-resonant scattering rate as a function of probe polarization components (top) and probe intensity (bottom) show the expected contribution from each transition to detection error near the range of experiment parameters. Nominal probe intensity used in the experiment of $I_+/I_{\text{sat}} = 0.40$ is used in the calculation of the top plot and is marked by a vertical line in the bottom plot. I_{sat} is the saturation intensity on the $|F = 4, m_F = 4\rangle \rightarrow |F' = 5', m'_F = 5'\rangle$ transition. Polarization fractions of $I_z = 1.5\%$ and $I_- = 0.007\%$ are used in the bottom plot.

$\tilde{I}_z = 1.5\%$, $\tilde{I}_- = 0.007\%$, and the intensity used in our main results in Sec. IV ($I_+/I_{\text{sat}} = 0.40$), we predict $R_{\text{dep}}/R_{\text{bright}} \approx 4.9 \times 10^{-7}$, or $\mathcal{R}_{\text{probe}} \approx 5.1 \times 10^{-5}$ after accounting for collection efficiency.

APPENDIX B: PREPARATION IN NONSTRETCHED ZEEMAN SUBLEVELS

While the stretched Zeeman-state sublevel is used in this paper to achieve maximum bright-state detection probability, other choices of Zeeman-state preparation are sometimes desirable, such as using the $m_F = 0$ “clock” states for magnetic insensitivity. The detection protocol presented here should also work well for other Zeeman states within the $F = 4$ manifold at the cost of a small, transient depumping probability during bright-state detection. This transient depumping would occur for even a perfect σ_+ detection beam because

TABLE II. Bright-state detection transient depump probability for a single scattering event (P_{dep, m_F}) and total depumping probability before reaching the stretched state (ε_{m_F}) when starting in the Zeeman sublevel m_F assuming pure σ_+ polarization, low B -field, and $I/I_{\text{sat}} = 0.40$.

m_F	-4	-3	-2	-1	0	1	2	3	4
$P_{\text{dep}, m_F} \times 10^4$	4.6	2.0	1.1	0.73	0.48	0.32	0.19	0.09	0
$\varepsilon_{m_F} \times 10^4$	9.2	5.5	3.9	2.8	2.1	1.4	0.91	0.44	0

the Clebsch-Gordan coefficient between $F = 4$ and $F' \neq 5$ is only zero for $m_F = 4$. The σ_+ probe beam quickly pumps an atom starting in $F = 4, m_F \neq 4$ into $F = 4, m_F = 4$; however, for all scattering events before the atom reaches the stretched state there is a chance of off-resonant scatter given by

$$P_{\text{dep}, m_F} = \left(\sum_{F' \neq 5} b_{F'} R_{\text{scat}, F', m'_F} \right) / R_{\text{scat}, 5', m'_F}. \quad (\text{B1})$$

Here $b_{F'}$ is the branching ratio to $F = 3$ and is listed in Table I, and R_{scat} is defined as it is in Eq. (A1), with the exception that the lower level can now be any m_F sublevel of the $F = 4$ ground-state manifold. We calculate P_{dep} for all Zeeman sublevels assuming perfect σ_+ polarization, 0 G B -field approximation, and the saturation parameter $I_+/I_{\text{sat}} = 0.40$ and record the results in Table II. The main difference between this calculation and that of the previous section is that now the full power of the probe beam can contribute to off-resonant scattering. Thus, the result depends much more on the overall probe intensity than the polarization purity (for small deviations from σ_+). We calculate the total depump probability before reaching the stretched state for an atom initialized in m_F by exploring the full outcome tree of each state-changing scattering event accounting for Zeeman-specific decay probabilities. It is also worth noting that if one considers *both* probe polarization impurity and transient depumping effects, there is a small increase to the depumping rates calculated in the previous section due to finite steady-state population in $|F = 4, m_F \neq 4\rangle$ Zeeman sublevels from polarization impurity that is then subject to transient depumping.

APPENDIX C: ADAPTIVE DETECTION FOR LOSS MITIGATION

In the main text, we emphasize techniques to mitigate various depumping mechanisms and achieve high-fidelity state detection. Here, we describe in more detail a technique to address a similarly important matter: atom retention in the trap after detection. We show that adaptive detection can reduce extraneous recoil heating, allowing for improved survival probability of bright state atoms.

Photon recoil from the near resonant probe beam causes a bright atom to undergo a random walk in momentum space, eventually allowing the atom to gain sufficient energy to overcome the trap depth [$U_0/k_b = 0.43(1)$ mK] and escape. Other heating mechanisms, such as dipole-force fluctuation heating [22] and ODT intensity fluctuation heating [42] are neglected

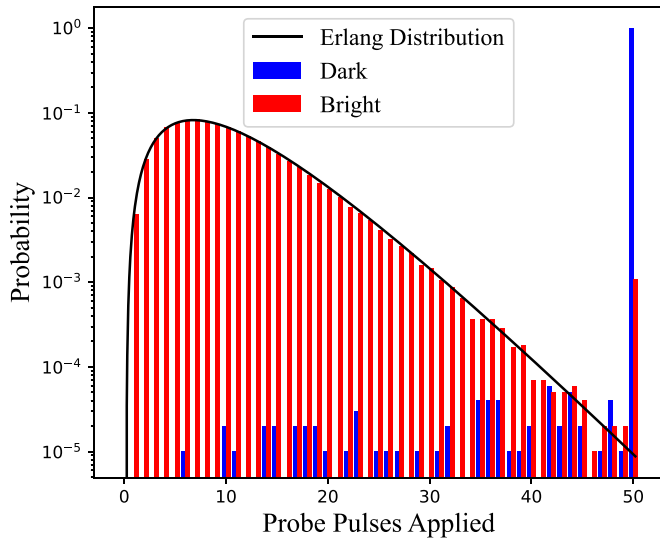


FIG. 7. We measure the wait time distribution for the bright and dark states using adaptive detection. 5- μ s probe pulses are applied until the threshold level of counts are recorded or the maximum possible detection time of 250 μ s is reached. The time distribution for the bright state (red bars) closely matches an Erlang distribution (black line), which is the expected distribution for the depump-free case. The discrepancy between the chance that bright atoms reach the maximum detection time ($0.11^{+0.03}_{-0.02}\%$) and the Erlang distribution at max time reveals the probability that bright atoms become dark before the threshold level of photons is collected. The time distribution for atoms prepared in the dark state (blue bars) is nearly unity at the maximum time bin. The combined effect of background counts on the detector and dark atoms becoming bright allows for small, but nonzero, probability of reaching threshold counts and stopping detection early when preparing in the dark state. These data were produced by recording the number of pulses applied when collecting data in Fig. 3.

here due to their small contributions on this experiment, as observed by the small ac Stark shift on the probe transition [43] and long (seconds scale), trap power independent, atom storage time, respectively. In a standard detection scheme, the mean number of counts collected from the bright state must be significantly higher than the threshold level to collect above-threshold counts from the bright state with high probability. This poses a problem when the recoil heating becomes comparable to the trap depth. For example, to achieve $\geq 99.9\%$ bright label probability from a Poisson count distribution by thresholding at three or more counts, the mean would need to be ≥ 11.2 counts. Dividing by our collection efficiency of $CE = 0.96(1)\%$ gives a requirement of $N_{\text{scat}} \approx 1170$ photons scattered on average. If we approximate the expected heating from photon recoil with the free atom case, a single resonant scattering event adds $\Delta E/k_b = 2T_{\text{rec}} \approx 2 * 0.2 \mu\text{K}$ per recoil event [22,23,35], such that the mean energy gain after single pulse detection would be 0.47 mK. This energy gain is greater than the trap depth, implying a significant loss probability due to detection.

However, if state labeling is determined entirely with thresholding, any extra light collected beyond the threshold level provides no additional information. Therefore, we can avoid much of the unnecessary recoil heating if we turn off

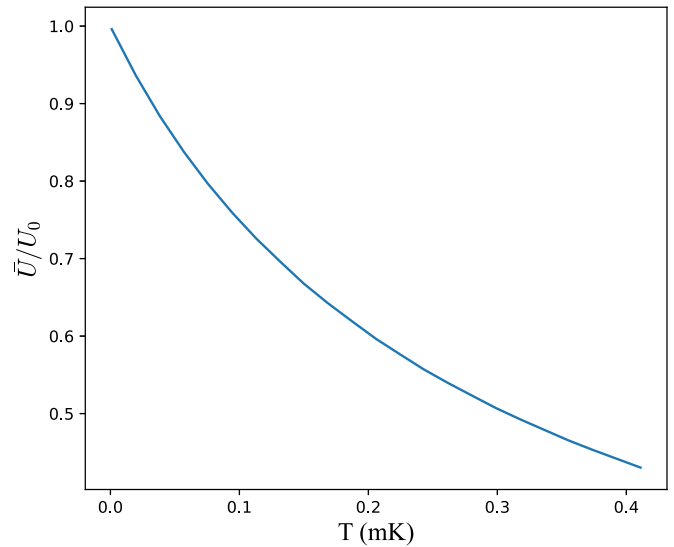


FIG. 8. Average trap intensity experienced by the atom decreases due to thermal wave-packet spread as the temperature of the atom increases. We approximate \bar{U}/U_0 for a range of temperatures up to the trap depth by calculating the overlap of a Gaussian potential with a thermal harmonic oscillator wave packet [44]. We use a trap depth of $U_0/k_b = 0.43(1)$ mK, a waist of $w_0 = 1.6 \mu\text{m}$, and numerically integrate over $\pm 4w_0$ and $\pm 4z_R$ in the radial and axial dimensions, respectively. When the atom temperature is significant compared to the trap depth, this reduction in effective intensity experienced by the atom should be accounted for when calculating both the two-photon depumping and single-photon off-resonant scattering mechanisms discussed in the text.

the detection light as soon as we reached the threshold level. In the ideal case of stopping the instant the threshold photon is received, the mean number of photons collected for a depump-free bright atom would simply be the threshold level, and thus the average temperature gain would be roughly a factor of 3/11.2 times lower than the constant probe time case, keeping the average energy gain below the trap depth.

We refer to this protocol as “adaptive detection,” and note that similar protocols were used on neutral atoms in Ref. [14] and on trapped ions in Refs. [25–29]. We implement such a scheme by applying a series of short (5 μ s) pulses until either the threshold number (three counts) are detected or we reach a total integrated probe duration of $t_d = 250 \mu\text{s}$. This maps the bright-state count distribution in Eq. (1) onto a nearly Erlang wait time (t) distribution with shape parameter equal to the detection threshold ($m = 3$): $f(t) \approx R_{\text{bright}}^3 t^2 e^{-R_{\text{bright}} t} / 2!$ shown in Fig. 7.

APPENDIX D: DERIVATION OF THE RAMAN RABI RATE FROM THE TRAP DEPTH

To calculate the Raman Rabi rate $\Omega_{\text{eff},F'}$ from a measured quantity, we find that $\Omega_{\text{eff},F'}$ can be derived from the trap depth, U_0 , of the far-detuned optical dipole trap, where

$$U_0 = \frac{\hbar \Omega_{D_2}^2}{4} \left(\frac{1}{\Delta_{D_2}} + \frac{f_{D_1}/f_{D_2}}{\Delta_{D_1}} \right). \quad (\text{D1})$$

Here, Ω_{D_2} is the nominal optical Rabi frequency of the linearly polarized trap light, and f_{D_1} and f_{D_2} are the oscillator strengths

TABLE III. Calculation parameters for each single-photon Rabi rate involved in two-photon depumping calculation. Dipole moments for each transition (d) are shown relative to that of the $6S_{1/2}$ to $6P_{3/2}$ transition (d_0) for comparison to the example calculation in the text. Values for d calculated with the Alkali Rydberg Calculator [45].

NL	J	F	m_F	$N'L'$	J'	F'	m'_F	Eq. (A3) Prefactor	$ d / d_0 $	$(-1)^{2F'+F-q+7}$	$\begin{bmatrix} J & I & F \\ F' & 1 & J' \end{bmatrix}_{6j}$	$C_{F,m_F,1,q}^{F',m'_F}$
6S	1/2	4	4	6P	3/2	5	5	$\sqrt{2/3}$	1.000	1	1/6	1
7S	1/2	4	4	6P	3/2	5	5	$\sqrt{2/3}$	1.023	1	1/6	1
8S	1/2	4	4	6P	3/2	5	5	$\sqrt{2/3}$	0.235	1	1/6	1
9S	1/2	4	4	6P	3/2	5	5	$\sqrt{2/3}$	0.124	1	1/6	1
6D	3/2	4	4	6P	3/2	5	5	$\sqrt{1/15}$	0.738	1	$\sqrt{7}/30$	1
6D	3/2	5	4	6P	3/2	5	5	$\sqrt{1/15}$	0.738	-1	$-3\sqrt{22}/110$	$-\sqrt{6}/6$
6D	5/2	4	4	6P	3/2	5	5	$\sqrt{2/5}$	0.721	1	$\sqrt{77}/330$	1
6D	5/2	5	4	6P	3/2	5	5	$\sqrt{2/5}$	0.721	-1	$-\sqrt{462}/330$	$-\sqrt{6}/6$
5D	3/2	4	4	6P	3/2	5	5	$\sqrt{1/15}$	1.126	1	$\sqrt{7}/30$	1
5D	3/2	5	4	6P	3/2	5	5	$\sqrt{1/15}$	1.126	-1	$-3\sqrt{22}/110$	$-\sqrt{6}/6$
5D	5/2	4	4	6P	3/2	5	5	$\sqrt{2/5}$	1.142	1	$\sqrt{77}/330$	1
5D	5/2	5	4	6P	3/2	5	5	$\sqrt{2/5}$	1.142	-1	$-\sqrt{462}/330$	$-\sqrt{6}/6$
7D	3/2	4	4	6P	3/2	5	5	$\sqrt{1/15}$	0.345	1	$\sqrt{7}/30$	1
7D	3/2	5	4	6P	3/2	5	5	$\sqrt{1/15}$	0.345	-1	$-3\sqrt{22}/110$	$-\sqrt{6}/6$
7D	5/2	4	4	6P	3/2	5	5	$\sqrt{2/5}$	0.340	1	$\sqrt{77}/330$	1
7D	5/2	5	4	6P	3/2	5	5	$\sqrt{2/5}$	0.340	-1	$-\sqrt{462}/330$	$-\sqrt{6}/6$
6S	1/2	4	4	6P	3/2	4	3	$\sqrt{2/3}$	1.000	1	$-\sqrt{21}/36$	$\sqrt{5}/5$
7S	1/2	4	4	6P	3/2	4	3	$\sqrt{2/3}$	1.023	1	$-\sqrt{21}/36$	$\sqrt{5}/5$
8S	1/2	4	4	6P	3/2	4	3	$\sqrt{2/3}$	0.235	1	$-\sqrt{21}/36$	$\sqrt{5}/5$
9S	1/2	4	4	6P	3/2	4	3	$\sqrt{2/3}$	0.124	1	$-\sqrt{21}/36$	$\sqrt{5}/5$
6D	3/2	4	4	6P	3/2	4	3	$\sqrt{1/15}$	0.738	1	$2\sqrt{3}/45$	$\sqrt{5}/5$
6D	3/2	5	4	6P	3/2	4	3	$\sqrt{1/15}$	0.738	-1	$\sqrt{7}/30$	$6\sqrt{55}/55$
6D	5/2	4	4	6P	3/2	4	3	$\sqrt{2/5}$	0.721	1	$\sqrt{33}/60$	$\sqrt{5}/5$
6D	5/2	5	4	6P	3/2	4	3	$\sqrt{2/5}$	0.721	-1	$-\sqrt{3}/15$	$6\sqrt{55}/55$
5D	3/2	4	4	6P	3/2	4	3	$\sqrt{1/15}$	1.126	1	$2\sqrt{3}/45$	$\sqrt{5}/5$
5D	3/2	5	4	6P	3/2	4	3	$\sqrt{1/15}$	1.126	-1	$\sqrt{7}/30$	$6\sqrt{55}/55$
5D	5/2	4	4	6P	3/2	4	3	$\sqrt{2/5}$	1.142	1	$\sqrt{33}/60$	$\sqrt{5}/5$
5D	5/2	5	4	6P	3/2	4	3	$\sqrt{2/5}$	1.142	-1	$-\sqrt{3}/15$	$6\sqrt{55}/55$
7D	3/2	4	4	6P	3/2	4	3	$\sqrt{1/15}$	0.345	1	$2\sqrt{3}/45$	$\sqrt{5}/5$
7D	3/2	5	4	6P	3/2	4	3	$\sqrt{1/15}$	0.345	-1	$\sqrt{7}/30$	$6\sqrt{55}/55$
7D	5/2	4	4	6P	3/2	4	3	$\sqrt{2/5}$	0.340	1	$\sqrt{33}/60$	$\sqrt{5}/5$
7D	5/2	5	4	6P	3/2	4	3	$\sqrt{2/5}$	0.340	-1	$-\sqrt{3}/15$	$6\sqrt{55}/55$
6S	1/2	4	4	6P	3/2	3	3	$\sqrt{2/3}$	1.000	1	1/12	$\sqrt{7}/3$
7S	1/2	4	4	6P	3/2	3	3	$\sqrt{2/3}$	1.023	1	1/12	$\sqrt{7}/3$
8S	1/2	4	4	6P	3/2	3	3	$\sqrt{2/3}$	0.235	1	1/12	$\sqrt{7}/3$
9S	1/2	4	4	6P	3/2	3	3	$\sqrt{2/3}$	0.124	1	1/12	$\sqrt{7}/3$
6D	3/2	4	4	6P	3/2	3	3	$\sqrt{1/15}$	0.738	1	$-\sqrt{7}/21$	$\sqrt{7}/3$
6D	5/2	4	4	6P	3/2	3	3	$\sqrt{2/5}$	0.721	1	$\sqrt{77}/84$	$\sqrt{7}/3$
5D	3/2	4	4	6P	3/2	3	3	$\sqrt{1/15}$	1.126	1	$-\sqrt{7}/21$	$\sqrt{7}/3$
5D	5/2	4	4	6P	3/2	3	3	$\sqrt{2/5}$	1.142	1	$\sqrt{77}/84$	$\sqrt{7}/3$
7D	3/2	4	4	6P	3/2	3	3	$\sqrt{1/15}$	0.345	1	$-\sqrt{7}/21$	$\sqrt{7}/3$
7D	5/2	4	4	6P	3/2	3	3	$\sqrt{2/5}$	0.340	1	$\sqrt{77}/84$	$\sqrt{7}/3$

TABLE IV. Effective Raman Rabi rates relative to V-type transition through the ground state for target level $|6P_{3/2}, F' = 4, m'_F = 3\rangle$.

Intermediate state	$\Omega_{\text{eff},4',i}/\Omega_{\text{eff},4',6S_{1/2}}$
$ 6S, J = 1/2, F = 4, m_F = 4\rangle$	1.000
$ 7S, J = 1/2, F = 4, m_F = 4\rangle$	-0.287
$ 8S, J = 1/2, F = 4, m_F = 4\rangle$	0.031
$ 9S, J = 1/2, F = 4, m_F = 4\rangle$	0.004
$ 6D, J = 3/2, F = 4, m_F = 4\rangle$	-0.197
$ 6D, J = 3/2, F = 5, m_F = 4\rangle$	-0.296
$ 6D, J = 5/2, F = 4, m_F = 4\rangle$	-0.518
$ 6D, J = 5/2, F = 5, m_F = 4\rangle$	1.381
$ 5D, J = 3/2, F = 4, m_F = 4\rangle$	0.012
$ 5D, J = 3/2, F = 5, m_F = 4\rangle$	0.018
$ 5D, J = 5/2, F = 4, m_F = 4\rangle$	0.038
$ 5D, J = 5/2, F = 5, m_F = 4\rangle$	-0.102
$ 7D, J = 3/2, F = 4, m_F = 4\rangle$	-0.002
$ 7D, J = 3/2, F = 5, m_F = 4\rangle$	-0.003
$ 7D, J = 5/2, F = 4, m_F = 4\rangle$	-0.007
$ 7D, J = 5/2, F = 5, m_F = 4\rangle$	0.019
Sum over states	1.09

for the D_1 and D_2 transitions. Typically, $f_{D_1}/f_{D_2} \approx 1/2$. The optical detunings Δ_{D_1} and Δ_{D_2} are defined by the center of gravity of the ground state and excited states (i.e., ignoring the hyperfine structure).

To relate Ω_{D_2} to the electric field amplitude, we perform a more detailed calculation according to Ref. [31] and find

$$\Omega_{D_2} = \sqrt{\frac{2}{9}} \frac{\mathcal{E}d}{\hbar}, \quad (\text{D2})$$

where \mathcal{E} is the electric-field amplitude of the linearly polarized trap light, and d is given by Eq. (A4). In our illustrative case under study, we have $\mathcal{E}_+ = \mathcal{E}_- = \mathcal{E}/\sqrt{2}$. Using the ground state as an example intermediate state, we substitute into Eq. (A3) to find the single-photon Rabi rates for each arm of the transition, $\Omega_{\pm,i} = \Omega_{F',m'_F,F,m_F}$:

$$\Omega_{F',m'_F,F,m_F} = \Omega_{D_2} \times \sqrt{\frac{3}{2}} (-1)^{2F'+F-q+7} \sqrt{(2J+1)(2F+1)} \\ \times \left\{ \begin{matrix} J & I & F \\ F' & 1 & J' \end{matrix} \right\}_{6j} C_{F,m_F,1,q}^{F',m'_F}. \quad (\text{D3})$$

Definitions in Eq. (D3) are the same as in Eq. (A3). Now, we can express $\Omega_{\text{eff},F',i}$ in terms of Ω_{D_2} by substituting into Eq. (2) to find

$$\Omega_{\text{eff},4',i} \Big|_{|i=6S_{1/2}} \approx a_{F',i} \frac{\Omega_{D_2}^2}{2\Delta_i} \Big|_{|i=6S_{1/2}}, \quad (\text{D4})$$

TABLE V. Effective Raman Rabi rates relative to V-type transition through ground state for target level $|6P_{3/2}, F' = 3, m'_F = 3\rangle$.

Intermediate state	$\Omega_{\text{eff},3',i}/\Omega_{\text{eff},3',6S_{1/2}}$
$ 6S, J = 1/2, F = 4, m_F = 4\rangle$	1.000
$ 7S, J = 1/2, F = 4, m_F = 4\rangle$	-0.287
$ 8S, J = 1/2, F = 4, m_F = 4\rangle$	0.031
$ 9S, J = 1/2, F = 4, m_F = 4\rangle$	0.004
$ 6D, J = 3/2, F = 4, m_F = 4\rangle$	-0.493
$ 6D, J = 5/2, F = 4, m_F = 4\rangle$	0.863
$ 5D, J = 3/2, F = 4, m_F = 4\rangle$	0.029
$ 5D, J = 5/2, F = 4, m_F = 4\rangle$	-0.064
$ 7D, J = 3/2, F = 4, m_F = 4\rangle$	-0.005
$ 7D, J = 5/2, F = 4, m_F = 4\rangle$	0.012
Sum over states	1.09

where $a_{F',i}$ is the product of all coefficients in Eq. (D3) for both arms of the Raman transition and $\Delta_i \approx \Delta_i - \delta_{F',5}$ since the optical detuning is much larger than the two-photon detuning ($|\Delta_i| \gg |\delta_{F',5}|$). Then, we may rearrange Eq. (D1) to read

$$\Omega_{D_2}^2 = \frac{4U_0}{\hbar} \left| \frac{\Delta_{D_1} \Delta_{D_2}}{\Delta_{D_1} + (f_{D_1}/f_{D_2})\Delta_{D_2}} \right|, \quad (\text{D5})$$

such that we can express the effective Raman Rabi rate directly in terms of the trap depth

$$\Omega_{\text{eff},F',i} = a_{F',i} \frac{2U_0}{\hbar \Delta_i} \left| \frac{\Delta_{D_1} \Delta_{D_2}}{\Delta_{D_1} + (f_{D_1}/f_{D_2})\Delta_{D_2}} \right|. \quad (\text{D6})$$

As a concrete example, we now provide numbers for the transition to final state $|6P_{3/2}, F' = 4, m'_F = 3\rangle$ through intermediate state $|i\rangle = |6S_{1/2}, F = 4, m_F = 4\rangle$, a V-type Raman transition through the ground state. Evaluation of Eq. (D3) for each arm of this transition yields $\Omega_{+,i} = \sqrt{\frac{3}{2}} \sqrt{\frac{1}{2}} \Omega_{D_2}$ and $\Omega_{-,i} = -\sqrt{\frac{3}{2}} \sqrt{\frac{7}{120}} \Omega_{D_2}$. Therefore,

$$a_{4',6S_{1/2}} = -\sqrt{\frac{21}{320}}, \quad (\text{D7})$$

and

$$\Omega_{\text{eff},4',6S_{1/2}} \approx 2\pi \times \left(-0.255 \frac{U_0}{h} \right). \quad (\text{D8})$$

Calculation for other intermediate states are done in the same fashion, and results are given in Tables III to V.

- [1] I. S. Madjarov, J. P. Covey, A. L. Shaw, J. Choi, A. Kale, A. Cooper, H. Pichler, V. Schkolnik, J. R. Williams, and M. Endres, *Nat. Phys.* **16**, 857 (2020).
[2] H. Levine, A. Keesling, G. Semeghini, A. Omran, T. T. Wang, S. Ebadi, H. Bernien, M. Greiner, V. Vuletić, H.

Pichler, and M. D. Lukin, *Phys. Rev. Lett.* **123**, 170503 (2019).

- [3] D. Bluvstein, H. Levine, G. Semeghini, T. T. Wang, S. Ebadi, M. Kalinowski, A. Keesling, N. Maskara, H. Pichler, M. Greiner, V. Vuletić, and M. D. Lukin, *Nature (London)* **604**, 451 (2022).

- [4] H. Bernien, S. Schwartz, A. Keesling, H. Levine, A. Omran, H. Pichler, S. Choi, A. S. Zibrov, M. Endres, M. Greiner, V. Vuletić, and M. D. Lukin, *Nature (London)* **551**, 579 (2017).
- [5] H. Labuhn, D. Barredo, S. Ravets, S. de Léséleuc, T. Macrì, T. Lahaye, and A. Browaeys, *Nature (London)* **534**, 667 (2016).
- [6] J. T. Zhang, Y. Yu, W. B. Cairncross, K. Wang, L. R. B. Picard, J. D. Hood, Y.-W. Lin, J. M. Hutson, and K.-K. Ni, *Phys. Rev. Lett.* **124**, 253401 (2020).
- [7] A. W. Young, W. J. Eckner, W. R. Milner, D. Kedar, M. A. Norcia, E. Oelker, N. Schine, J. Ye, and A. M. Kaufman, *Nature (London)* **588**, 408 (2020).
- [8] M. Endres, H. Bernien, A. Keesling, H. Levine, E. R. Anschuetz, A. Krajenbrink, C. Senko, V. Vuletic, M. Greiner, and M. D. Lukin, *Science* **354**, 1024 (2016).
- [9] D. Barredo, S. de Léséleuc, V. Lienhard, T. Lahaye, and A. Browaeys, *Science* **354**, 1021 (2016).
- [10] D. Ohl de Mello, D. Schäffner, J. Werkmann, T. Preuschoff, L. Kohfahl, M. Schlosser, and G. Birkl, *Phys. Rev. Lett.* **122**, 203601 (2019).
- [11] D. Barredo, V. Lienhard, S. de Léséleuc, T. Lahaye, and A. Browaeys, *Nature (London)* **561**, 79 (2018).
- [12] Alkaline earth and helium-like atoms have become an increasingly popular choice as well, with the most recent progress in strontium and ytterbium, which have narrow line optical clock transitions.
- [13] A. Fuhrmanek, R. Bourgain, Y. R. P. Sortais, and A. Browaeys, *Phys. Rev. Lett.* **106**, 133003 (2011).
- [14] M. J. Gibbons, C. D. Hamley, C.-Y. Shih, and M. S. Chapman, *Phys. Rev. Lett.* **106**, 133002 (2011).
- [15] M. Kwon, M. F. Ebert, T. G. Walker, and M. Saffman, *Phys. Rev. Lett.* **119**, 180504 (2017).
- [16] M. Martinez-Dorantes, W. Alt, J. Gallego, S. Ghosh, L. Ratschbacher, Y. Völzke, and D. Meschede, *Phys. Rev. Lett.* **119**, 180503 (2017).
- [17] J. Bochmann, M. Mücke, C. Guhl, S. Ritter, G. Rempe, and D. L. Moehring, *Phys. Rev. Lett.* **104**, 203601 (2010).
- [18] R. Gehr, J. Volz, G. Dubois, T. Steinmetz, Y. Colombe, B. L. Lev, R. Long, J. Estève, and J. Reichel, *Phys. Rev. Lett.* **104**, 203602 (2010).
- [19] E. Deist, Y.-H. Lu, J. Ho, M. K. Pasha, J. Zeiher, Z. Yan, and D. M. Stamper-Kurn, *Phys. Rev. Lett.* **129**, 203602 (2022).
- [20] T.-Y. Wu, A. Kumar, F. Giraldo, and D. S. Weiss, *Nat. Phys.* **15**, 538 (2019).
- [21] T. Grünzweig, A. Hilliard, M. McGovern, and M. F. Andersen, *Nat. Phys.* **6**, 951 (2010).
- [22] M. Martinez-Dorantes, W. Alt, J. Gallego, S. Ghosh, L. Ratschbacher, and D. Meschede, *Phys. Rev. A* **97**, 023410 (2018).
- [23] D. J. Wineland and W. M. Itano, *Phys. Rev. A* **20**, 1521 (1979).
- [24] With a gold mirror to minimize polarization distortion.
- [25] D. B. Hume, T. Rosenband, and D. J. Wineland, *Phys. Rev. Lett.* **99**, 120502 (2007).
- [26] A. H. Myerson, D. J. Szwer, S. C. Webster, D. T. C. Allcock, M. J. Curtis, G. Imreh, J. A. Sherman, D. N. Stacey, A. M. Steane, and D. M. Lucas, *Phys. Rev. Lett.* **100**, 200502 (2008).
- [27] S. D. Erickson, J. J. Wu, P.-Y. Hou, D. C. Cole, S. Geller, A. Kwiatkowski, S. Glancy, E. Knill, D. H. Slichter, A. C. Wilson, and D. Leibfried, *Phys. Rev. Lett.* **128**, 160503 (2022).
- [28] S. Crain, C. Cahall, G. Vrijsen, E. E. Wollman, M. D. Shaw, V. B. Verma, S. W. Nam, and J. Kim, *Commun. Phys.* **2**, 97 (2019).
- [29] S. L. Todaro, V. B. Verma, K. C. McCormick, D. T. C. Allcock, R. P. Mirin, D. J. Wineland, S. W. Nam, A. C. Wilson, D. Leibfried, and D. H. Slichter, *Phys. Rev. Lett.* **126**, 010501 (2021).
- [30] We initially considered the possibility of multiple state change events, however, that is suppressed to first order in $t_d R_{\text{dep}}$.
- [31] W. Happer, Y.-Y. Jau, and T. Walker, *Optically Pumped Atoms* (Wiley-VCH, Weinheim, Germany, 2010).
- [32] Note that, in the case that the atom temperature is significant compared to the trap depth, atomic wave packet broadening should also be considered when calculating the trap off-resonant scattering rate. The numeric correction can be estimated from Fig. 8.
- [33] We used a Thorlabs PAX1000 polarimeter for this measurement.
- [34] D. A. Steck, Cesium D Line Data (1998, Revision 2.2.1, 21 November 2019), <http://steck.us/alkalidata/>.
- [35] D. A. Steck, Quantum and Atom Optics, <http://steck.us/teaching> (revision 0.13.21, 5 June 2023).
- [36] These data were collected with fiber-coupled fluorescence and are meant only to illustrate the difference between π - and σ -polarized trap lights, not to be an example of detection fidelity with optimal settings.
- [37] We note that the development and integration of single-photon avalanche diode (SPAD) array sensors could potentially provide a suitably fast signal to perform adaptive detection on an array of atoms if combined with individual site addressing of single-qubit rotation or detection beams [46–51].
- [38] B. Nikolov, E. Diamond-Hitchcock, J. Bass, N. L. R. Spong, and J. D. Pritchard, *Phys. Rev. Lett.* **131**, 030602 (2023).
- [39] W. Huie, L. Li, N. Chen, X. Hu, Z. Jia, W. K. C. Sun, and J. P. Covey, Repetitive readout and real-time control of nuclear spin.
- [40] H. J. Metcalf and P. van der Straten, *Laser Cooling and Trapping* (Springer-Verlag, New York, 1999).
- [41] For calculations using representation of reduced matrix elements, we find $\langle 6P_{3/2} || er || 6S_{1/2} \rangle = \sqrt{2/3}d$ for the convention used in Refs. [35,52], and $\langle 6P_{3/2} || er || 6S_{1/2} \rangle = \sqrt{4/3}d$ for the convention used in Refs. [31,53,54].
- [42] T. A. Savard, K. M. O'Hara, and J. E. Thomas, *Phys. Rev. A* **56**, R1095 (1997).
- [43] The trap wavelength is nearly magic for the probe transition.
- [44] R. P. Feynman, *Statistical Mechanics: A Set of Lectures* (Westview, Boulder, CO, 1972).
- [45] N. Šibalić, J. Pritchard, C. Adams, and K. Weatherill, *Comput. Phys. Commun.* **220**, 319 (2017).
- [46] N. A. W. Dutton, I. Gyongy, L. Parmesan, S. Gnechhi, N. Calder, B. R. Rae, S. Pellegrini, L. A. Grant, and R. K. Henderson, *IEEE Trans. Electron Devices* **63**, 189 (2016).
- [47] M. Gersbach, J. Richardson, E. Mazaleyrat, S. Hardillier, C. Niclass, R. Henderson, L. Grant, and E. Charbon, *Solid-State Electron.* **53**, 803 (2009).

- [48] I. Gyongy, N. Calder, A. Davies, N. A. W. Dutton, R. R. Duncan, C. Rickman, P. Dalgarno, and R. K. Henderson, *IEEE Trans. Electron Devices* **65**, 547 (2018).
- [49] J. Richardson, R. Walker, L. Grant, D. Stoppa, F. Borghetti, E. Charbon, M. Gersbach, and R. K. Henderson, in *Proceedings of the 2009 IEEE Custom Integrated Circuits Conference* (IEEE, New York, 2009), pp. 77–80.
- [50] K. Morimoto, A. Ardelean, M.-L. Wu, A. C. Ulku, I. M. Antolovic, C. Bruschini, and E. Charbon, *Optica* **7**, 346 (2020).
- [51] N. C. Jackson, R. K. Hanley, M. Hill, F. Leroux, C. S. Adams, and M. P. A. Jones, *SciPost Phys.* **8**, 038 (2020).
- [52] D. M. Brink and G. R. Satchler, *Angular Momentum* (Oxford University Press, New York, 1962).
- [53] D. A. Varshalovich, A. N. Moskalev, and V. K. Khersonskii, *Quantum Theory of Angular Momentum* (World Scientific, Singapore, 1988).
- [54] F. Le Kien, P. Schneeweiss, and A. Rauschenbeutel, *Eur. Phys. J. D* **67**, 92 (2013).